Strengthening by High Densities of Nanometer-Size Precipitates: Oxides in Ni

DAVID M. FOLLSTAEDT, JAMES A. KNAPP, and SAMUEL M. MYERS

We have measured the yield strengths of Ni samples having high densities of nanometer-size precipitates. Surface layers containing NiO or γ-Al_2O_3 precipitates were formed in Ni specimens by ion implanting O alone or O and Al, with subsequent annealing. The yield strengths of the layers were obtained through nanoindentation in conjunction with finite-element simulations. The yield strengths of the Ni alloys were combined with earlier data for O-implanted Al and compared to predictions of a recent treatment of the Orowan mechanism, in which dislocations loop around precipitates and bypass them. The strengths vary with changes in precipitate microstructure, as predicted, and conform to the theory in absolute magnitude to within a factor of 1.5. This agreement extends over broad microstructural ranges: precipitate sizes from ~1 to 20 nm, volume fractions from 0.05 to 0.30, densities from $4 \times 10^{16}/cm^3$ to as high as $\sim 10^{20}/cm^3$, edge-to-edge spacings as small as 1.4 nm, two precipitated phases, and two metal matrices with shear moduli differing by a factor of 3. Ion implantation increases near-surface yield strengths to as high as 5 GPa, suggesting that this treatment may be useful for hardening the surfaces of Ni components in micro-electromechanical systems.

I. INTRODUCTION

SHEAR-RESISTANT precipitates in metals impede the motion of dislocations, which are believed to bypass the particles by bowing around them and reconnecting on the downstream side, leaving behind a circumscribing loop. This strengthening mechanism was initially considered by Orowan,[1] who identified the separation (λ) between precipitates as a key parameter controlling the critical resolved shear stress (CRSS):

$$\tau = G\mathbf{b}/\lambda \qquad [1]$$

Here, τ is the additional required stress for propagation of a dislocation with a Burgers vector of **b** on a slip plane through the field of precipitates in a metal with a shear modulus of G. The theoretical evaluation of this mechanism has been refined by others.[2,3] These later evaluations show that the correct precipitate spacing for this strengthening mechanism is the edge-to-edge distance between precipitates, and for the remainder of this article, we assign this meaning to λ.

Key experiments examining precipitate hardening were performed with Cu single crystals having well-defined slip systems and BeO[4] or SiO_2[5] precipitates. The experimental CRSS values from these two experiments were found to be in reasonable agreement with the Orowan mechanism.[6] These experiments and others cover a range of precipitate diameters from ~5 to 100 nm and volume fractions of 0.0033 to 0.041. The Orowan mechanism in Eq. [1] points toward nanometer-size precipitate separations as a microstructural regime offering increased strength, which can be achieved with high numbers of small precipitates per unit volume. However, there are few experiments with precipitates having sizes and separations of only a few nanometers.

Ion implantation offers the ability to produce this special type of microstructure. This technique can athermally introduce isolated atoms of an insoluble species into a host metal.[7] Since the diffusivities of many species are low at room temperature, the implanted atoms remain at their implanted depth and the solid solubility can be exceeded to produce a thermodynamic driving force for precipitation. The numerous lattice defects produced during implantation provide nucleation sites that can result in a high density of nanometer-size precipitates. For species having a finite atomic mobility, precipitation can occur during implantation. For other elements, a subsequent anneal may be required, or annealing may allow thermally evolved microstructures to be investigated. Moreover, implanted concentrations of tens of atomic percentages can be achieved for light elements, so that high volume fractions of the second phase can precipitate. Thus, ion implantation can form high densities of very small precipitates only a few nanometers apart. In this limit, the strengthening mechanisms and their mathematical evaluations might change, perhaps because dislocation segments in close proximity interact differently, or because precipitates become shearable when reduced in diameter to $<\sim 2$ nm. Furthermore, with sizes and precipitate spacings of only a few nanometers, discrete atom effects might become important and produce changes. Additional experiments are, therefore, needed to understand strengthening in this regime.

In earlier work, we formed nanometer-size Al_2O_3 precipitates in Al by O implantation[8,9] and found very high yield strengths, up to ~3 GPa. The work reported here examines the strengthening of ion-implanted Ni by high densities of hard oxides. We chose Ni since its shear modulus differs from that of Al by 3 times. Two methods were used to produce precipitation: (1) O alone was implanted to form NiO precipitates a few nanometers in diameter, and (2) both Al and O were implanted and reacted to form γ-Al_2O_3 precipitates only 1 to 2 nm in diameter. Both precipitated phases

DAVID M. FOLLSTAEDT, and JAMES A. KNAPP, Principal Members of Technical Staff, Radiation–Solid Interactions Department, and SAMUEL M. MYERS, Senior Scientist, Nanostructure and Semiconductor Physics Department, are with Sandia National Laboratories, Albuquerque, NM 87185-1056. Contact e-mail: dmfolls@sandia.gov

Manuscript submitted April 15, 2002.

can increase the yield strength of the Ni matrix to ~5 GPa; however, the γ-Al_2O_3 precipitates are much more thermally stable, and the strength is retained upon annealing. We used ion-beam analysis to determine the depth-dependent concentration profiles of the implanted species and transmission electron microscopy (TEM) to characterize the size of precipitates within the implanted layer.

We previously compared results from a subset of these Ni alloys and those of Al to an earlier evaluation of the Orowan CRSS for propagation of dislocations through a close-packed array of precipitates centered in the glide plane.[10] The measured strengths varied as predicted for changes in precipitate size and volume fraction. However, a more complete treatment is needed to account for the statistical placement of particles about the glide plane and to consider a Taylor factor,[11] which relates the yield strength to the CRSS in metals with randomly oriented grains by projecting applied stress onto their glide planes. Here, we evaluate the mechanical properties of a larger set of Ni alloys and compare them and the Al results to a recent theoretical evaluation that includes dislocation interactions, random statistical placement of the precipitates, and elastic anisotropy.[6] The observed yield strengths vary with precipitate microstructure and metal matrix, as predicted, and also agree quantitatively with the theory to within a factor of 1.5, similar to the agreement found[6] for the results with Cu single crystals.[4,5]

The intrinsic mechanical properties of thin implanted layers require special techniques to evaluate. We have developed a method[8,12] to determine the yield strength of thin hard layers on a soft substrate. Ultralow-load indentation ("nanoindentation") is done to a depth partway through the layer, and the force applied to the indenter and the elastic stiffness of the specimen are measured as functions of depth. The force and stiffness are simulated with finite-element modeling to account for the mechanical response of both the layer and the substrate. Since the mechanical properties of the substrate are independently known, the properties of the layer can be varied until a good fit to the combined mechanical response is achieved. The numerical methods used for our recent evaluations have been discussed in detail in several publications. [10,12,13]

Our experiments and analyses focus on the centers of the implanted layers, which are designed to have a nearly constant composition over a depth interval greater than 100 nm by the use of multiple ion implantations at several energies. Since the number of precipitates per unit volume exceeds $10^{19}/cm^3$, precipitates will overlap in projected images, and accurate assessment of their density and spacings is not directly possible with TEM imaging. Instead, the composition is used with the measured precipitate size to calculate the volume fraction of precipitates, the number of precipitates per unit volume (N_v, the "number density"), and the average edge-to-edge spacing, each for the center of the implanted layer, assuming that all of the oxygen has precipitated. Moreover, results from finite-element modeling are most sensitive to the yield strength of this central region and are relatively insensitive to the details of how strength falls off at the back of the layers to the value for bulk Ni. Therefore, we have produced a set of specimens with concentrations of 4 to 16 at. pct in the center of the implanted layers and have compared the yield strengths of these regions to those predicted by the Orowan model for their precipitate microstructures.

In addition to understanding strengthening for these extreme microstructures, our work is a "proof-of-principle," demonstrating that Ni can be significantly strengthened beyond levels typically achieved for engineering alloys. For instance, the yield strength of nickel-based superalloys like NIMONIC PE16 is less than 1 GPa[14] and that of bearing steels is ~2 GPa, both less than the ~5 GPa strengths determined in this study. Moreover, ion-implantation treatments of the type examined in this work may prove useful for hardening the surfaces of Ni components in micro-electromechanical systems.

II. METHODS USED

A. *Ion Implantation*

The implanted alloys were formed in Ni of nominal 99.99 pct purity, which had been annealed for 2 hours at 1000 °C in high vacuum. This anneal produced observable grain relief and grain sizes between 200 and 500 μm. Disks ~1-mm thick were implanted for indentation testing, while foils 260-μm thick were used for examination of implanted alloy microstructures with TEM. All the implantations were done at room temperature in a turbomolecular-pumped vacuum system at a pressure of 3×10^{-5} Pa (2×10^{-7} Torr). The alloys were formed by combining implantations at multiple energies to produce a broad region of approximately uniform composition using ion fluences chosen with guidance from the composition profiles predicted by simulations using the Transport of Ions in Matter (TRIM) Monte Carlo codes.[15] A composite TRIM profile, using the energies and fluences given in Table I for an alloy with 16 at. pct O extending over an ~120-nm depth interval, is shown in Figure 1. This Ni specimen with nominal 16 at. pct O is referred to as Ni-16 pct O. Alloys with 8 at. pct O used the same energies with fluences scaled by one-half. An additional Ni-8 pct O specimen was also subsequently annealed 2 hours at 550 °C to examine the mechanical properties with ripened precipitates.

A second implantation schedule formed alloys with composition profiles of O and Al that overlap each other to a depth of ~200 nm. The implantation energies and fluences were again chosen from TRIM simulations[15] to achieve the desired profiles, such as for for the alloy with 8 at. pct each of O and Al (Ni-8 pct Al + O), as given in Table II. The implantations were intended to promote the formation of Al_2O_3 by using nearly equal amounts of Al and O, so that adequate Al is present to react with all the O during annealing. Alloys with 4 at. pct concentrations were also examined.

Table I. Implantation Energies and Fluences Used to Form the Ni-16 Pct O Alloy

Species	Energy	Fluence
O^+	50 keV	5.3×10^{16} O/cm^2
	100 keV	5.9×10^{16} O/cm^2
	140 keV	15.1×10^{16} O/cm^2
	Total O:	26.4×10^{16} O/cm^2

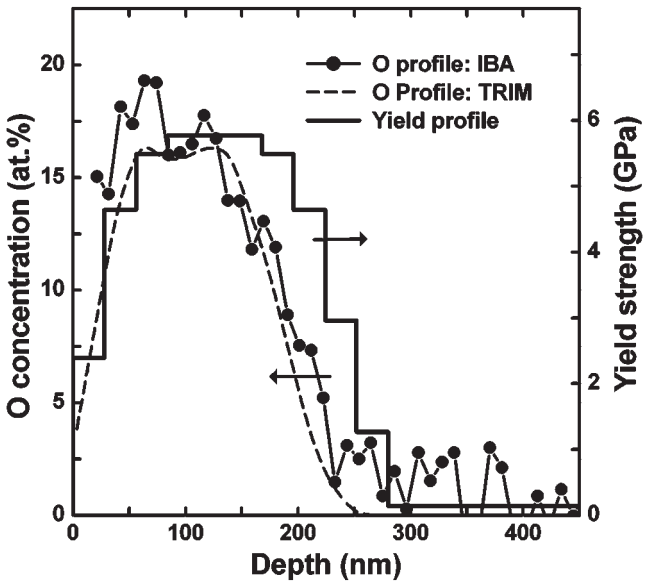

Fig. 1—Oxygen depth profiles for Ni-16 pct O implanted according to the schedule in Table I. Dashed line: simulated profile obtained with the TRIM Monte Carlo program.[15] Connected data points: profile measured using ion backscattering analysis (IBA). Also shown as a solid, blocked line is the profile of yield strength *vs* depth providing the best fit with finite-element modeling to the nanoindentation data for this specimen.

Table II. Implantation Energies and Fluences Used to Form the Ni-8 Pct Al + O Alloy

Species	Energy	Fluence
O^+	50 keV	3.0×10^{16} O/cm^2
	100 keV	3.3×10^{16} O/cm^2
	150 keV	8.5×10^{16} O/cm^2
	Total O:	14.8×10^{16} O/cm^2
Al^+	50 keV	2.0×10^{16} Al/cm^2
	100 keV	2.0×10^{16} Al/cm^2
	180 keV	10.0×10^{16} Al/cm^2
	Total Al:	14.0×10^{16} O/cm^2

B. *Ion-Beam Analysis*

Ion backscattering analysis[16] was used to profile the concentration of implanted species with a depth resolution generally ~10 nm. Special procedures were required to profile Al and O since they have lower atomic masses than Ni, causing their associated backscattering yields to overlap the yield from the Ni substrate. The concentration profiles of O and Al in Ni were determined from the energy spectra of backscattered He ions by using the known scattering cross sections and energy-loss rates for He passing through these elements. In particular, two separate backscattering spectra were obtained from each alloy, using He^4 ions at two different energies: 2.5 MeV for a higher depth resolution, and 8.6 MeV for an enhanced non-Rutherford cross section providing higher sensitivity to O. An iterative analysis was used with the Simulation of Nuclear Reaction Analysis (SIMNRA) program[17] to obtain depth profiles for both Al and O concentrations that fit the two spectra. To obtain a depth scale, an atomic density equal to that of pure Ni was assumed for the implanted layer. An example of a final profile deduced by this method is shown in Figure 1. This profile agrees well with that predicted by the TRIM calculation.

C. *Transmission Electron Microscopy*

A 200 kV instrument with 2.7 Å point-to-point resolution was used to image the NiO and Al_2O_3 precipitates. The astigmatism corrections of the objective lens were adjusted to compensate for distortions in its magnetic field induced by the magnetic Ni specimens. Plan-view TEM specimens were prepared by backthinning the Ni foils with jet electropolishing using a nitric acid solution. The plan-view orientation gave the best electron diffraction patterns for identifying the precipitated phases and was used for determining precipitate sizes, principally by dark-field imaging with a precipitate reflection.

Cross-sectional TEM revealed the microstructure as a function of depth. To prepare the specimen, a 2-mm-wide piece of Ni foil was epoxied between pieces of Si, and a 2.3-mm-diameter cylinder centered on the foil was ultrasonically cored. The Ni foil must be contained entirely within the core, since it resists ultrasonic abrasion and would otherwise erode the coring tool. The core was epoxied into a 3-mm-o.d. brass tube, and disks were sliced from it. The resulting brass ring around the disk helps maintain its structural integrity, which is important because we have not found adhesives that bond Si strongly to Ni. The disks were metallographically polished and thinned with the dimpling instrument using diamond paste. Final thinning was done by ion milling with 3.5 keV argon ions at a 4 deg glancing incidence. The Si thinned more rapidly, leaving an unsupported strip of Ni, but a usable thin area for TEM at the implanted surface was, nonetheless, obtained.

A second imaging technique was found to be useful with the cross-sectional specimens. The specimen was tilted to minimize diffraction contrast, and the objective lens was underfocused to produce Fresnel contrast, highlighting the precipitates as light central regions with a dark ring around them.[18] This occurs because the precipitates have a lower average atomic number than the Ni matrix. The observed precipitate contrast was confined to the implanted depth interval expected from TRIM. Cross-sectional imaging thus confirmed precipitation and gave a measure of precipitate sizes. This method was especially useful for imaging precipitates in Ni-4 pct Al + O, for which dark-field contrast was less effective.

To obtain the volume fraction of the precipitated phase, we assume that all the implanted O atoms have precipitated. For the case of O implantation only, we show subsequently that the phase NiO precipitates, with one reacted Ni atom per O atom. The volume fraction of NiO precipitates in the fcc Ni matrix is then calculated by

$$f = \frac{(2c/\rho_a\,(\mathrm{NiO}))}{((1-2c)/\rho_a\,(\mathrm{Ni}) + 2c/\rho_a\,(\mathrm{NiO}))} \qquad [2]$$

where c is the atomic fraction of O, and ρ_a is the atomic density for the indicated phase. Using the lattice constants for these crystal structures,[19] we obtain the values $\rho_a(\mathrm{NiO}) = 1.098 \times 10^{23}$ atoms/cm^3 and $\rho_a(\mathrm{Ni}) = 9.142 \times 10^{22}$ atoms/cm^3.

For the case of implanting both Al and O and reacting them to form γ-Al_2O_3 precipitates, accounting for 2 Al atoms per 3 O atoms, the corresponding expression is

$$f = \frac{((5/3)c/\rho_a\,(Al_2O_3))}{((1 - (5/3)c)/\rho_a\,(Ni) + (5/3)c/\rho_a\,(Al_2O_3))} \quad [3]$$

where the atomic density of γ-Al_2O_3 is $\rho_a(Al_2O_3) = 1.082 \times 10^{23}$ atoms/cm^3.

To obtain the edge-to-edge spacing between precipitates, we assume that all precipitates are spherical, with an average diameter of d, and place them in a close-packed fcc array. The resulting edge-to-edge separation between precipitates is

$$\lambda = \left(\sqrt[3]{\frac{\pi}{3f\sqrt{2}}} - 1 \right) d \quad [4]$$

The number of precipitates per unit volume is then given by

$$N_v = \frac{6f}{\pi d^3} \quad [5]$$

D. *Nanoindentation*

Nanoindentation was used to determine the mechanical properties of implanted Ni. The force needed to push a three-sided Berkovich diamond tip into the specimen was recorded continuously as a function of depth.[20–24] The displacement and load resolutions during indentation are about 0.02 nm and 50 nN, respectively. Ten indentations were done on each specimen at different positions, and the results were averaged at each depth increment, with the standard deviations of the averaged values taken as the errors. We found good sensitivity to the implanted layer by indenting partway through it to a depth of 160 nm. The contact stiffness, which is the change in force per unit depth during unloading, was also measured. The continuous stiffness measurement technique uses an oscillatory displacement of ~1 nm superimposed on the indentation, to obtain stiffness values over the entire indented depth.[22] The force generally depends upon both the elastic and plastic properties of the specimen, while the stiffness depends almost entirely upon the elastic properties. Obtaining both force and stiffness to be fitted as functions of depth was important for accurate evaluations of the yield strength by finite-element modeling, since the evaluations are complicated by the shallowness of the implanted layers and the depth variation of mechanical properties, which change with composition. We note that the indented depth and the width of deformed material (~1 μm) greatly exceed the precipitate sizes and their separations, so that the response of the material reflects the bulk properties of the implanted layer, not discrete precipitate effects.

E. *Finite-Element Modeling*

To extract the properties of the implanted alloy, finite-element methods are used to model the combined response of the implanted layer and substrate.[10,12,13] This approach also has the important ability to account for the depth dependence of the implanted layer's mechanical properties, which vary with composition. We use the commercial large-strain, finite-element code ABAQUS/Standard,[25] along with our own software utilities for generating meshes that model the specimen with depth-dependent material descriptions specific to each specimen, as discussed in detail in Reference 12. Most of our calculations use a two-dimensional, axisymmetric model for ease and speed of calculation. In selected cases, we have implemented full three-dimensional calculations that account for the true three-sided shape of the indenter tip and found that the yield strength varies by only a few percentages from that of the axisymmetric approximation.

The Ni substrate is treated as an isotropic elastic-plastic solid with a yield strength of $Y = 0.15$ GPa, a Young's elastic modulus of $E = 204$ GPa, and a Poisson's ratio of $\nu = 0.312$.[26] The code calculates deformations using a von Mises yield criterion. To account for work hardening, the stress-strain (σ-ε) relationship for Ni under uniaxial compression is taken to be

$$\sigma = E\varepsilon \qquad \text{for } \varepsilon \le Y_0/E \quad [6a]$$

$$\sigma = K\varepsilon^n \qquad \text{for } \varepsilon \ge Y_0/E$$

where Y_0 is the initial yield point, K is the strength coefficient, and n is the work-hardening exponent.[27] Continuity at $\varepsilon = Y_0/E$ is assured by using

$$K = Y_0(E/Y_0)^n \quad [6b]$$

We further define the yield strength in this parameterization as the stress at 0.002 strain on the (σ-ε) curve. For the Ni substrate, $n = 0.27$.[28] This exponential formulation of work hardening differs slightly from that in our previous finite-element modeling,[10,12] where we assumed a linear approximation to the hardening after the yield point. Additional considerations for modeling the Ni substrate are treated in the evaluation of Ni-16 pct O, as discussed in Section IV.

The diamond tip is modeled as a purely elastic solid with a Young's modulus of $E = 1140$ GPa and a Poisson's ratio of $\nu = 0.07$.[22] The mesh describing the diamond indenter includes rounding of the tip obtained from calibration of its cross-sectional area as a function of depth, which was determined by indenting into the well-understood reference material, fused silica.

The yield strength and elastic modulus of the implanted layer were varied to fit the observed force and stiffness. The Poisson's ratio in the implanted layer is assumed to be $\nu = 0.312$, as for pure Ni. Given the small separation (<5 nm) between precipitates and the close proximity of dislocations to multiple precipitates (~2 nm), using work hardening to treat interactions between dislocations within the implanted layer does not appear justified. Moreover, our experimental assessment and numerical evaluation are not able to discern separately such strain-related hardening within the implanted layer. Therefore, we model the implanted layer as a simple elastic-plastic solid with no strain hardening. The yield strength is assumed to vary across the implanted layer in approximate conformance with the concentration profiles, as seen in the example in Figure 1. We varied the width of the strength profile by as much as ±25 pct and examined the resulting fits of simulations to the data. The quality of the fit to the data was optimized by choosing a width somewhat wider than the O profile as seen in Figure 1, but was

relatively insensitive to the detailed way that the profile decreases from its maximum to the value for the pure Ni substrate. The maximum yield strength in the center of the profile was found to be the primary factor determining how well the data are fit; its fitted value changed by about 10 pct with changes in the width of the profile. The central value deduced from the best fit was then compared to predictions of the Orowan model using the precipitate microstructures.

III. COMPOSITIONAL AND MICROSTRUCTURAL ANALYSES

A. *Ni implanted with O*

The O depth profile for Ni-16 pct O obtained from ion-backscattering analysis is shown in Figure 1. The implanted O profile agrees well with that predicted by the TRIM calculation except for depths <25 nm, where the resolution of ion-beam analysis limits accuracy. The implanted concentration greatly exceeds the solid solubility of O in Ni,[29] and precipitation is expected since short-range diffusion is likely to be sufficient due to the excess point defects created during implantation. The profile obtained for Ni-8 pct O scaled from that in Figure 1 as expected.

Precipitation did occur during implantation, and the phase was identified with electron diffraction. Figure 2(a) is an [001] zone-axis electron diffraction pattern with a square array of intense fcc Ni reflections, obtained in plan view from from Ni-8 pct O. Radially inward from each Ni reflection is a weak reflection due to the precipitates. The lattice spacings of fcc Ni (a_0 = 3.524 Å)[19] were used as internal standards to calibrate the scale of the pattern, thus giving the lattice spacings of the precipitated phase within ~1 pct. These values match the lattice spacings of fcc (NaCl-type) NiO,[19] whose lattice constant is 18.5 pct larger than that of Ni. The Miller indices of precipitate reflections are the same as those of their nearby Ni reflections, *i.e.*, the (200) NiO reflection is found just inside the (200) fcc Ni. This match demonstrates that the cubic axes of NiO align parallel to those of the Ni lattice, *i.e.*, the two phases have a "cube-on-cube" orientational relation. This alignment is found in other precipitated alloys, including O-implanted fcc Al in which cubic γ-Al_2O_3 precipitates form.[30]

Dark-field imaging with the NiO reflections in Ni-8 pct O illuminates a dense dispersion of fine precipitates 1.5 to 3.5 nm in diameter, as seen in Figure 2(b). Their small size indicates a high nucleation density, as expected from the many atomic displacements and resulting lattice defects produced by the implantation. The observed orientation probably gives a low free energy for the NiO nuclei.[31] For instance, if the nuclei were ~1 nm in size, near that of the smallest precipitates, the overall lattice mismatch with the matrix (~0.185 nm) would be less than the Burgers vector of Ni (**b** = 0.249 nm). The nucleus would then be coherent and have an interfacial energy that is expected to be lower. Assuming that all the O is in spherical NiO precipitates with an intermediate diameter of 2.5 nm and using the value of 8.5 at. pct O measured in the center of the implanted layer, the volume fraction of NiO is calculated to be f = 0.146 and the precipitate density is $1.8 \times 10^{19}/cm^3$. The edge-to-edge separation between neighboring precipitates can be calculated by assuming they are in a close-packed

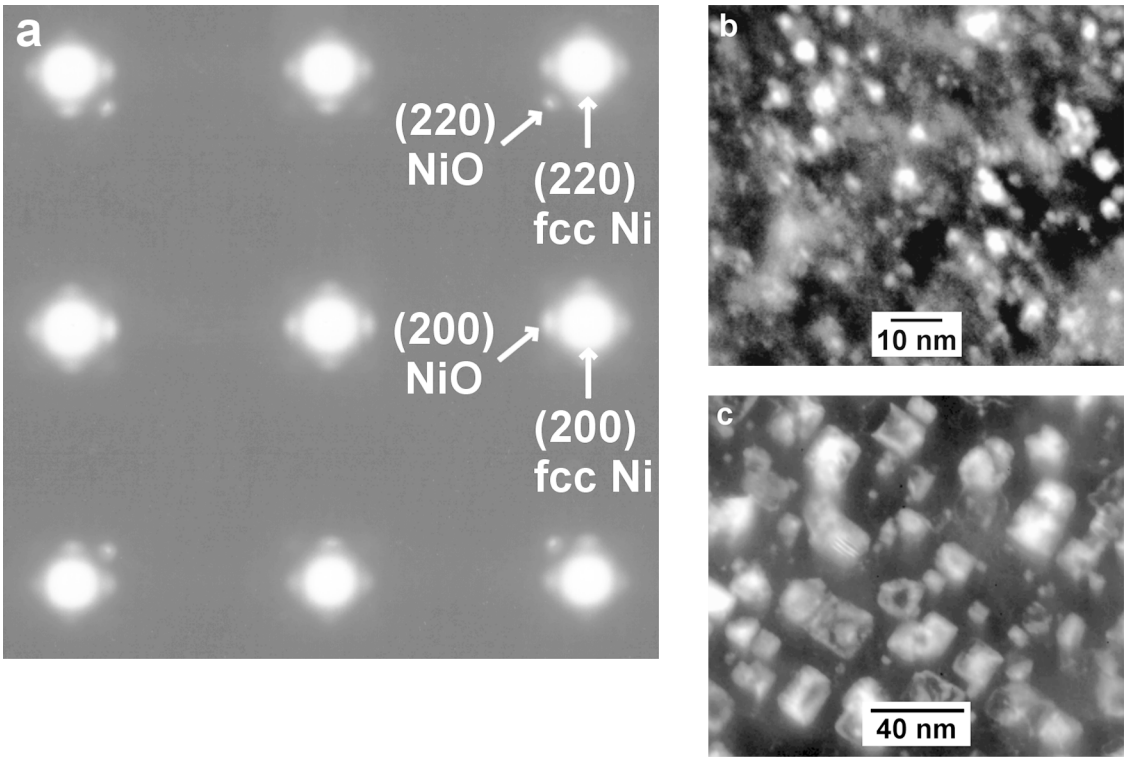

Fig. 2—Plan-view TEM characterizing NiO precipitates in Ni-8 pct O. (*a*) [001] electron diffraction pattern from specimen in the as-implanted condition (no anneal). (*b*) Dark-field image of the NiO precipitates in the as-implanted condition, obtained with a precipitate reflection. (*c*) Dark-field image of NiO precipitates after annealing for 2 h at 550 °C; note that this image is enlarged less than that in (b).

array, giving an average separation of $\lambda = 1.8$ nm. These values demonstrate the extremely refined microstructural regime in which we are investigating precipitate strengthening.

After annealing Ni-8 pct O for 2 hours at 550 °C, the O depth profile was changed insignificantly from that just after implantation. To understand the lack of change, we extrapolated the diffusivity ($\mathcal{D}$) of O from published work[29] to obtain $\mathcal{D} = 1.9 \times 10^{-12}$ cm^2/s at 550 °C, giving an expected diffusion distance of $\sqrt{\mathcal{D}t} = 1200$ nm. At this temperature, the solid solubility of O in Ni is only 2.4×10^{18}/cm^3.[29] The amount of O that could then diffuse from the alloy layer and into the substrate is calculated to be only $\sim 3 \times 10^{14}$ O/cm^2, a small fraction of the amount implanted, which is consistent with the unchanged depth profile. Transport in the metal at the solubility concentration restricts the evolution of the profile, because most of the O is fixed in NiO precipitates and unable to diffuse in solid solution.

With this anneal, larger precipitates with a greater range of sizes were formed by ripening, as seen in the dark-field image of Figure 2(c). Electron diffraction again identified the phase as NiO, with sharper reflections due to the increased sizes; their orientation in the Ni matrix is unchanged. Figure 2(c) shows the precipitates near the [001] orientation. They appear cuboidal in shape, reflecting their cubic lattice. The dominant facets are {100}, which apparently provide low interfacial energy between NiO and fcc Ni.[31] The distribution of edge lengths was measured and found to have an average value of 13.5 nm, with a root-mean-squared (rms) variation of 6.2 nm. For these sizes, the overall lattice mismatch with the matrix is several Burgers vector lengths, and the particles are said to be semicoherent since misfit dislocations must be present. The volume fraction $f = 0.146$ gives a density of 3.7×10^{16}/cm^3 and a separation of $\lambda = 18$ nm. We calculate the average volume of a precipitate to be 3900 nm^3, and for the theoretical treatment of strengthening which follows, we use an effective diameter for a sphere of equal volume: 19.6 nm.

Ni-16 pct O was also examined after implantation. NiO precipitates again formed and are seen in Figure 3 to be rather uniform in size: the average diameter is 7.0 nm with an rms variation of 1.2 nm. This diameter is 2 to 4 times larger than that for as-implanted Ni-8 pct O and the volume of individual precipitates is one order of magnitude more, whereas the implanted O concentration is only twice as much. Using 17 at. pct O from the measured profile in Figure 1, the volume fraction of NiO is 0.30, the highest examined in this study. The calculated density of spherical precipitates is then 1.7×10^{18}/cm^3, with a separation of $\lambda = 2.5$ nm. The lower density compared to Ni-8 pct O indicates that some precipitates existing after the first half of the 16 pct O implantation were enlarged during the second half, and some were dissolved or incorporated into larger ones. The final precipitates are large enough that they are semicoherent.

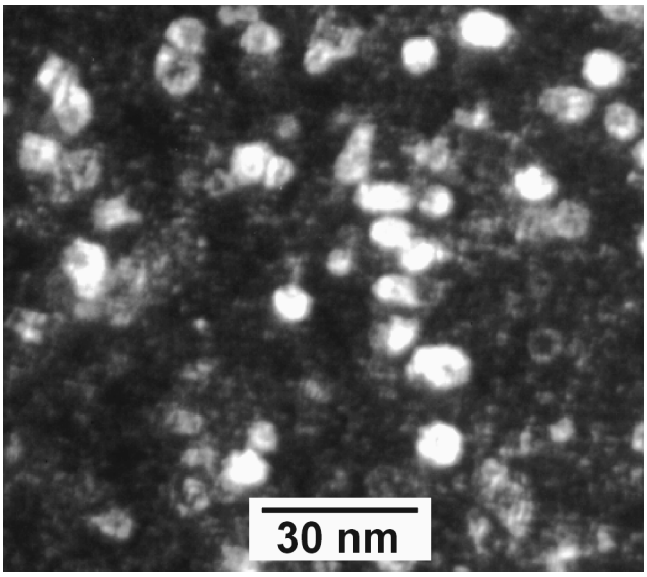

Fig. 3—Plan-view, dark-field image showing larger NiO precipitates in Ni-16 pct O in the as-implanted condition, obtained with a precipitate reflection.

B. *Ni Implanted with O and Al*

A Ni-8 pct Al + O specimen was characterized in the as-implanted condition. The TEM images and diffraction patterns indicated the presence of two precipitated phases, NiO and a spinel phase, either $NiAl_2O_4$ or γ-Al_2O_3. Precipitates were also detected in a Ni-4 pct Al + O specimen after implantation, but were not identified because their diffraction was weaker. The microstructures and fitted mechanical properties for both compositions are listed in Table III, with details available in Reference 10. Since the presence of two types of precipitates would hinder accurate interpretation of mechanical properties, the yield strengths of specimens with Al and O in the as-implanted condition were not used in the following theoretical analysis. Annealing was, therefore, used to provide Al and O atoms with sufficient diffusion distances to encounter each other, react, and form precipitates. The mechanical properties of these annealed specimens were compared to predictions of the Orowan mechanism (as detailed subsequently).

A separate specimen was implanted under conditions chosen to demonstrate the reaction of Al and O in Ni during annealing. In this case, 1×10^{17} Al/cm^2 was implanted at 50 keV and 2×10^{17} O/cm^2 was implanted at 320 keV. These fluences were high to increase the signals of Al and O, and single energies were used to produce concentrations more localized in depth. As seen in Figure 4(a), the O concentration peaks at 300 nm, far below the Al implanted at lower energy, which is near the surface. The specimen was subsequently annealed for 2 hours at 800 °C to demonstrate the reaction by transport of the reactants over significant distances. The resulting depth profiles, seen in Figure 4(b), have changed dramatically; the Al and O now overlap each other. At 800 °C, both species were quite mobile and migrated toward each other, demonstrating that the exothermic reaction of O and Al[32] operates in the Ni matrix to form Al_2O_3. If the Al and O were not reacting, they would have diffused independently into the substrate.

Depth profiles in Ni-8 pct Al + O, obtained after annealing for 2 hours at 550 °C, are shown in Figure 5. The two profiles overlap closely to form an alloy with nearly uniform composition extending to 200 nm in depth, with

Table III. Implanted Compositions, Thermal Treatments, Precipitate Microstructures, and Resulting Mechanical Properties

Specimen Conditions		Precipitate Microstructures					Fitted Mechanical Properties*			Predicted
Composition	Anneal	Phase	Size (nm)	f	N_v (cm^{-3})	λ (nm)	Y (GPa)	E (GPa)	H (GPa)	CRSS (GPa)
Pure Ni	none	—	—	—	—	—	0.15	204 ± 11	—	—
Ni-impl. Ni**	none	—	—	—	—	—	0.85 ± 0.11	225 ± 29	2.7 ± 0.3	—
Ni-16 pct O	none	NiO	7.0 ± 1.2	0.30	1.7×10^{18}	2.5	5.77 ± 0.37	263 ± 18	14.5 ± 1.0	2.65 ± 0.30
							5.20 ± 0.38	227 ± 20	13.3 ± 1.1	—
Ni-8 pct O	none	NiO	1.5 to 3.5	0.146	1.8×10^{19}	1.8	5.11 ± 0.43	234 ± 15	13.1 ± 1.0	2.60 ± 0.35
	2 h 550 °C	NiO	13.5 ± 6.2†	0.146	3.7×10^{16}	18	1.38 ± 0.11	228 ± 23	4.1 ± 0.4	0.65 ± 0.15
Ni-8 pct Al + O	none	mixed‡	2,7 to 10	—	—	—	5.11 ± 0.29	265 ± 18	13.5 ± 0.8	
							5.05 ± 0.24	249 ± 12	13.1 ± 0.6	
	2 h 550 °C	γ-Al_2O_3	1 to 2	0.108	6.1×10^{19}	1.4	4.15 ± 0.30	255 ± 27	11.3 ± 1.0	2.60 ± 0.30
Ni-4 pct Al + O	none	mixed‡	1 to 1.5	—	—	—	—	—	—	—
	2 h 550 °C	γ-Al_2O_3	≈1.5	0.053	3.0×10^{19}	2.1	3.39 ± 0.28	221 ± 21	9.3 ± 0.8	1.60 ± 0.15

*The indicated uncertainties in mechanical properties reflect the statistical reproducibility of the indentation data and uncertainties in the fitting procedures used for evaluation.

**1.5×10^{16} Ni/cm^2 was implanted at room temperature into high-purity Ni at 300 keV.

†Edge length of the cuboidal precipitates.

‡Interpreted to be a mixture of spinel phases (Al_2O_3 or $NiAl_2O_4$) and NiO.

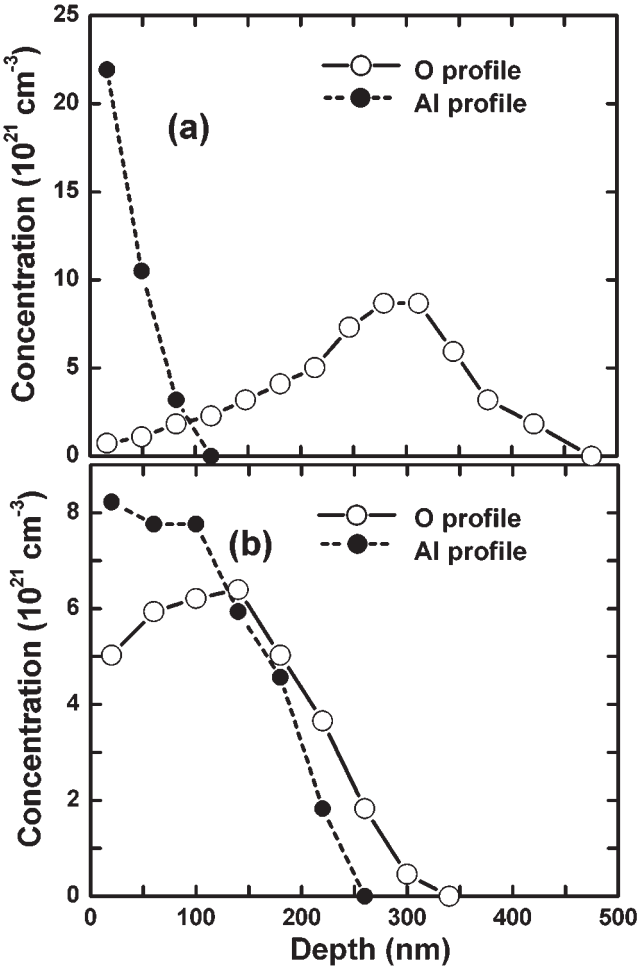

Fig. 4—Oxygen and Al depth profiles in a special specimen designed to demonstrate their reaction to form Al_2O_3 in Ni. Specimen was implanted with 1×10^{17} Al/cm^2 at 50 keV and 2×10^{17} O/cm^2 at 320 keV. (*a*) Profiles for the as-implanted condition (no anneal), and (*b*) profiles after annealing 2 h at 800 °C. Note the difference in vertical scales between the two figures.

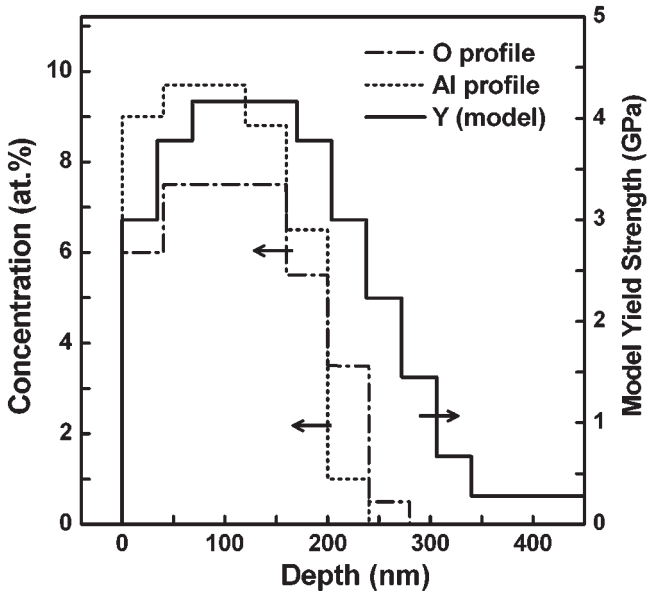

Fig. 5—Oxygen (dot-dash) and Al (dashed) depth profiles in Ni-8 pct O + Al implanted according to Table II, after annealing 2 h at 550 °C. Also shown as a solid, blocked line is the profile of yield strength *vs* depth providing the best fit with finite-element modeling to the nanoindentation data for this specimen.

maximum concentrations of 9.7 at. pct Al and 7.5 at. pct O. Before annealing, the O profile extended about 25 nm deeper. Thus, some implanted O migrated to overlap the Al during the anneal, indicating that O and Al also react in Ni at 550 °C, as confirmed subsequently by electron diffraction. The 2-hour anneal at 550 °C was chosen to allow sufficient atomic mobility to form Al_2O_3 while nearly retaining the uniform composition profiles designed with the TRIM calculation. Extrapolation from the measured diffusivities of Al in Ni[33,34] at higher temperatures predicts a value of only $\mathcal{D} = 3.0 \times 10^{-17}$ cm^2/s at 550 °C. During the anneal, Al is expected to diffuse only $\sqrt{\mathcal{D}t} = 5$ nm, in agreement with its unchanged

distribution, whereas O can diffuse up to 1200 nm.[29] Thus, O moves to react with Al, but the Al is sufficiently mobile to diffuse the short distances needed to form nanometer-size precipitates.

After this anneal, Ni-8 pct Al + O shows fine precipitates, as seen with an underfocused condition in the cross-sectional image in Figure 6. The precipitates extend to a depth of ~240 nm, in agreement with the Al and O profiles in Figure 5. Because of their high density ($N_v = 6.1 \times 10^{19}/cm^3$, as shown subsequently), they appear very dense in the projected TEM image of a specimen that is ~0.1-μm thick. Nonetheless, individual precipitates can be distinguished. Fewer precipitates are seen in the depth interval between 240 and 300 nm, and none are seen at greater depths. The precipitated phase was identified with electron diffraction in plan view. The [0–13] zone-axis diffraction pattern in Figure 7(a) and other orientations show weak reflections just inside those of fcc Ni. Using the Ni reflections as internal standards, the precipitate lattice spacings given in Table IV were obtained. Two spacings, 1.975 and 1.395 Å, match γ-Al_2O_3 closely but differ from the nearest spacings of NiO by ~5 pct, several times the accuracy of the measurement. The nearest spacings of $NiAl_2O_4$ are also outside the error range of the measured spacings.

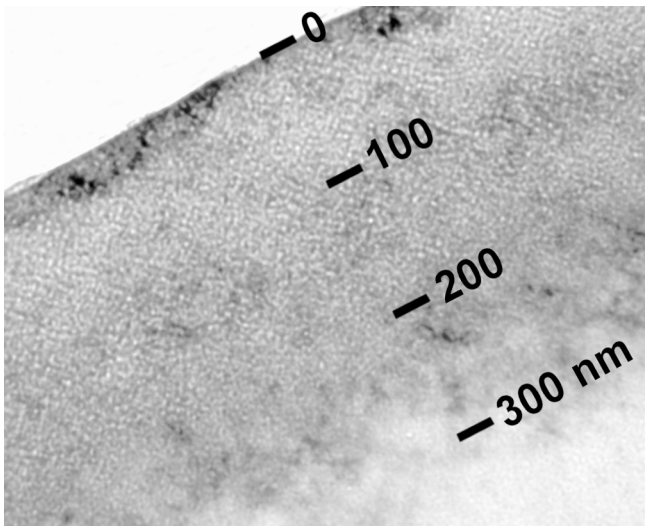

Fig. 6—Cross-sectional, bright-field TEM image of Ni-8 pct O + Al after annealing 2 h at 550 °C, showing a high density of γ-Al_2O_3 precipitates in the expected depth interval below the surface. Imaged in an underfocused condition to enhance the contrast of precipitates, which appear as light areas surrounded by a dark ring.

The positions and intensities of the precipitate reflections confirm the identification of γ-Al_2O_3 and give additional insight into its formation and atomic structure. The γ-Al_2O_3 (400) reflection is inside the (200) reflection of Ni in Figure 6, indicating the cube-on-cube orientation. The doubling of the indices relative to Ni is due to the ordered structure of γ-Al_2O_3. This spinel phase has an underlying fcc lattice of O^{-2} ions, with Al^{+3} ions in interstitial positions.[35] The O^{-2} lattice constant (3.95 Å) is one-half of that of the ordered γ-Al_2O_3 phase and differs from that of fcc Ni by only 12 pct. Some reflections of γ-Al_2O_3 listed in Table IV are not observed, such as (220). The (440) reflection is more intense because it results from the underlying O^{-2} lattice, whereas the (220) reflection is related to the ordered positions of Al^{+3} interstitials and is weaker. Our not detecting such reflections may be due to incomplete ordering of the interstitials in γ-Al_2O_3, as found for this phase in O-implanted Al.[30] The third measured lattice spacing in Table IV, 2.40 Å, fits all three phases within ~1 pct. The (311) reflection is one of the most intense γ-Al_2O_3 reflections and is seen in Figure 7(a) in alignment with (311) fcc Ni reflections but at one-half the radial distance, as expected. Notably, NiO precipitates

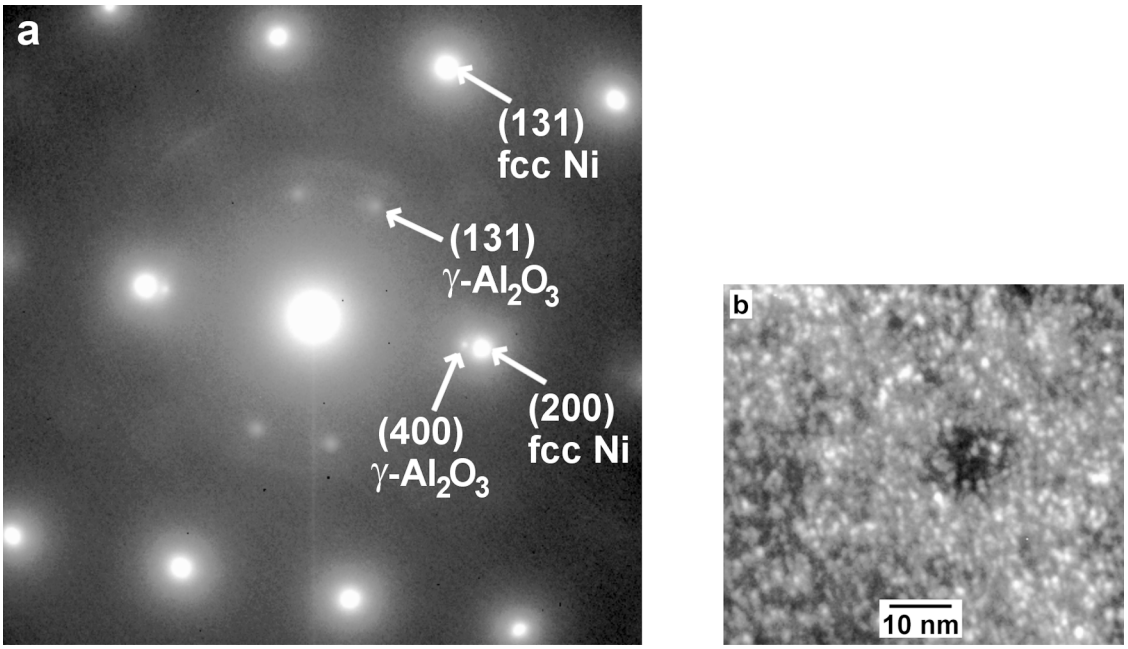

Fig. 7—Plan-view TEM characterizing γ-Al_2O_3 precipitates in Ni-8 pct O + Al after annealing 2 h at 550 °C. (*a*) [0–13] electron diffraction pattern showing weak γ-Al_2O_3 reflections and intense fcc Ni reflections. (*b*) Dark-field image of the γ-Al_2O_3 precipitates.

Table IV. Lattice Spacings and Indices for Phases in Ni Implanted with O and Al.

NiO*	$NiAl_2O_4$**	γ-Al_2O_3†	Ni(Al.O) observed‡
—	4.65 Å (111)	4.56 Å (111)	—
—	2.846 Å (220)	2.80 Å (220)	—
2.41 Å (111)	2.427 Å (311)	2.39 Å (311)	2.40 ± 0.015 Å
—	—	2.28 Å (222)	—
2.088 Å (200)	2.013 Å (400)	1.977 Å (400)	1.975 ± 0.01 Å
—	1.549 Å (511)	1.520 Å (511)	—
1.476 Å (220)	1.423 Å (440)	1.395 Å (440)	1.395 ± 0.01 Å

*Face-centered cubic phase, NaCl-type, a_o = 4.177 Å. ICDD PDF card 04-0835.[19]
**Cubic spinel phase, a_o = 8.048 Å. ICDD PDF card 10-0339.[19]
†Cubic phase, closely related to spinel structures, a_o = 7.90 Å. ICDD PDF card 10-0425.[19]
‡Ni implanted with nominal 8 at. pct Al and O, annealed 2 h at 550 °C.

would not have a reflection at this position, again confirming the identification of γ-Al_2O_3.

The hexagonal α-Al_2O_3 phase (corundum) is slightly more stable than γ-Al_2O_3,[35] but the γ phase apparently forms in Ni because of its cubic symmetry and close lattice matching. The O^{-2} sublattice can be coherent with the Ni lattice for small precipitates 1 to 2 nm in diameter, like those illuminated in the dark-field image of Figure 7(b). This small size reflects the high density of nucleation sites and the strongly exothermic reaction of Al and O. The thermal stability of these small γ-Al_2O_3 precipitates contrasts sharply with the larger NiO precipitates that ripened during the same anneal. For Ni-8 pct Al + O, the measured O concentration is 7.5 at. pct,[10] giving a volume fraction of 10.8 pct. Using an intermediate diameter of 1.5 nm gives a precipitate density of $6.1 \times 10^{19}/cm^3$ and $\lambda = 1.4$ nm.

A Ni-4 pct Al + O specimen was also annealed for 2 hours at 550 °C and examined with cross-sectional TEM. The underfocused image showed ~1.5 nm precipitates in the implanted depth interval. Due to the lower concentration, we were unable to get accurate diffraction data, but since 4 at. pct greatly exceeds the expected solid solubilities of O, the exothermic reaction of Al and O very probably occurred to produce γ-Al_2O_3. The lower O concentration gives a volume fraction of 0.053 and a number density of $3.0 \times 10^{19}/cm^3$ with $\lambda = 2.1$ nm. The precipitate size is essentially unchanged from 8 pct, but the density is reduced by one-half.

IV. EVALUATION OF MECHANICAL PROPERTIES

A. *Ni Implanted with O Only*

Figures 8(a) and (b) show the force and stiffness, respectively, for Ni-16 pct O during indentation. An indenter force of 1.7 mN is needed to reach 160 nm in this specimen. Shown for comparison are data for well-annealed, pure Ni. The forces initially required at shallow depths for Ni-16 pct O exceed those for untreated Ni by ~3 times. At ~50 nm, however, the force for the implanted specimen shows a change in slope to a more linear depth dependence and an almost constant offset above that for Ni. The initially higher force for Ni-16 pct O reflects the high strength and hardness of the implanted surface layer, whereas the break in curvature near 50 nm is due to the increasing influence

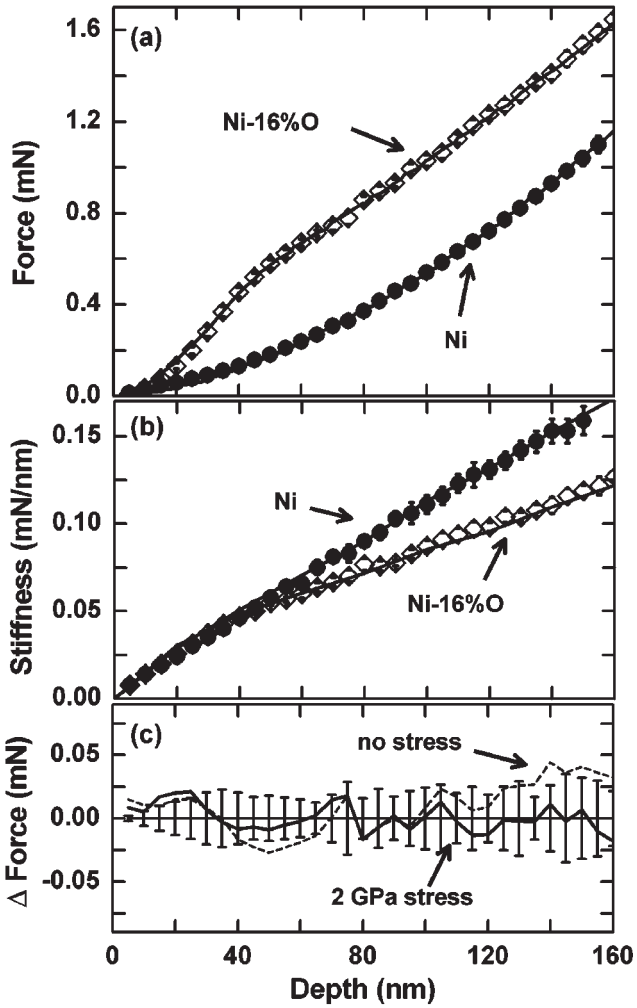

Fig. 8—Nanoindentation force and stiffness data from Ni-16 pct O alloy in the as-implanted condition and data for pure Ni. (*a*) Indenter force as a function of depth for Ni-16 pct O and for unimplanted Ni, along with finite-element simulations. (*b*) Stiffness as a function of depth for Ni-16 pct O and for unimplanted Ni, along with finite-element simulations. (*c*) Differences between indentation force data and simulations of force *vs* depth, shown on expanded vertical scale.

of the softer Ni substrate as the indented depth becomes an appreciable fraction of the layer thickness. The constant offset from Ni beyond ~70 nm indicates that the hard surface layer is being pushed ahead of the indenter into the sub-

strate, which is supporting the additional load required for added increments of depth.

The stiffness data in Figure 8(b) for Ni-16 pct O are initially slightly higher than those of Ni, then drop below them for depths >50 nm. This drop does not indicate that the elastic properties of the implanted layer have deteriorated, but can be understood by considering the area in contact with the indenter for a hard layer on a soft substrate. As the layer is pressed into the substrate, the contact area is smaller than for pure Ni. Since stiffness is proportional to the square root of the contact area,[12] the measured values are lower, as verified by finite-element modeling.

This specimen has the highest volume fraction of precipitates and the highest strength layer examined in this study. Modeling its nanoindentation data is, thus, somewhat more exacting and provides a good example of our approach to deducing the mechanical properties of implanted layers. We first consider whether a special feature seen with nanoindentation of pure Ni applies to implanted Ni. We[13] and others[36] have found that the apparent strength and hardness of untreated Ni are higher near the surface, *e.g.*, $Y_{surf} = 0.33$ GPa, *vs* 0.15 GPa for bulk Ni. These increases are attributed to the "indentation-size effect"[37] commonly observed in well-annealed metals.[38,39,40] This effect is believed to result from strain gradients in the metal beneath the indenter, which, in turn, lead to additional dislocations with geometries appropriate for accomodating deformation at the surface.[41] These additional dislocations increase hardness near the surface. In our earlier work,[13] we modeled untreated Ni near the surface, with a yield strength that decreased from the surface value to the bulk value over a depth of 1 μm, to mimic the increased hardness. Here, we compare using that graded yield strength for the Ni substrate beneath the implanted layer to using a constant, bulk value of pure Ni. Both models used the profile for yield strength within the implanted layer shown in Figure 1, with its maximum value being adjusted to obtain the best fit to the data in each case. The finite-element simulation using uniform bulk properties in the substrate gave a much better fit to the data than that for the graded yield strength, which gave results well outside the error limits for depths ≥100 nm. The uniform-substrate model gave a fitted yield strength of 5.88 GPa. This choice of models for the substrate was less apparent from the data for the other implanted Ni specimens, but, in light of the previous findings, a uniform substrate yield strength was chosen for them also. This choice gives yield strengths ~10 pct higher than those found with the graded yield strength.

It is our belief, based on physical considerations and experimental observations, that the numerous dislocations present after implantation and the small separation between precipitates (18 to 1.4 nm) relative to the indentation depth (up to 160 nm) preclude indentation-size effects in our nanoindentation data. Since both the depth and lateral (~1 μm) scales of the indentation extend over many precipitate spacings, the mechanical properties we deduce are believed to be representative of a bulk material with the same microstructure.

The difference (ΔF) between the calculated force and the data values is shown on an expanded scale in Figure 8(c), with the data error bars being placed at $\Delta F = 0$. Detailed examination of the fit with the constant substrate yield strength discussed earlier (dashed curve) shows that it passes through most error bars, but is slightly below them near the break in slope at 40 to 60 nm and is just above them at greater depths (130 to 160 nm). This comparison suggests that our model could be improved. In separate experiments, O was implanted into Ni films deposited on steel plates. The implanted Ni film was seen to bulge and break loose from the steel, indicating that O implantation produces compressive stresses in Ni. Stress values up to the yield strength could be sustained in the implanted layer; here, we considered compressive stresses that track the strength profile (Figure 1) with a maximum value of 2 GPa, which is ~35 pct of the yield strength. Including compressive stress in the model gives a simulation (solid curve) that fits the force data in Figure 8(c) well at all depths, and the systematic deviations seen without compressive stress are absent. Independently knowing that compressive stress is present and obtaining the improved fit suggest that it is appropriate to include stress in the model, although we do not have sufficient sensitivity to quantify it accurately. However, the resulting fitted yield stress, 5.77 ± 0.37 GPa, is only 2 pct less than that obtained previously without including stress, and, therefore, compressive stress was not included in modeling the other specimens with lower strengths. A second Ni-16 pct O specimen was also evaluated and gave a somewhat smaller yield strength, 5.20 ± 0.38 GPa.

Nanoindentation data for as-implanted Ni-8 pct O are very similar to those in Figure 8, as shown in Figures 5 and 6 of Reference 10. The data were fitted using the procedures identified previously, and a yield strength of 5.11 ± 0.43 GPa was obtained, somewhat less than the values for Ni-16 pct O. An optimum fit to these data required a slightly thicker yield-strength profile than that in Figure 1, extending to 340 nm.

As a check on our assigning the increased strengths to the presence of precipitates, a Ni specimen was ion implanted with Ni to produce lattice damage without altering the composition. Implantation of 1.5×10^{16} N/cm^2 at 300 keV was calculated by TRIM[15] to produce a peak in the irradiation damage of the Ni lattice of 65 displacements per atom, several times that calculated for the O implantations. The high Ni^+ energy places this peak at 50 nm in depth, with damage extending as deep as 150 nm. Indentation and modeling of this implanted layer gave a yield strength of 0.85 ± 0.11 GPa. The yield strengths for the unannealed O-implanted Ni specimens exceed this value by about 6 times, confirming our assignment of the increased strength to precipitation and ruling out strengthening due simply to irradiation damage.

The force data for Ni-8 pct O are greatly reduced after annealing for 2 hours at 550 °C, but exceed those for untreated Ni, as shown in Reference 10. This change is due to the ripening, which produced fewer, larger precipitates with greater separations and softened the implanted layer. A greatly reduced yield strength of 1.32 ± 0.11 GPa was determined. In this specimen, the lattice damage produce by implantation is expected to have greatly recovered, and its yield strength exceeds that of the Ni-implanted specimen anyway. Its yield strength can, therefore, be confidently attributed to precipitate strengthening.

The fitted yield-strength and modulus values for all the specimens are listed in Table III. The stated error limits are obtained from a statistical treatment of the variability in force measurements and the differences between measured and

fitted values at each depth.[12] As the previous discussion demonstrates, the fitted values are modestly influenced by our modeling assumptions. All together, our experiences with modeling and fitting implanted layers[10,12,13] and with repeating experiments (Table III) indicate that any additional systematic errors in yield strengths due to our evaluation techniques give an absolute uncertainty of ~10 pct.

B. *Ni Implanted with Al and O*

Figures 9(a) and (b) show the force and stiffness data, respectively, for nanoindentation of Ni-8 pct Al + O after annealing for 2 hours at 550 °C; data for pure Ni are reproduced for comparison. The Ni-8 pct Al + O data are similar in magnitude and trend to those for Ni-16 pct O. The specimen was modeled using the treatments discussed previously for O-implanted Ni. The optimum fitted profile of yield strength extended slightly deeper than that in Figure 1, similar to the profile in Figure 1 of Reference 10. For this specimen, cross-sectional TEM images using diffraction contrast (not shown) show some dislocations extending a bit deeper than the precipitates. These dislocations are residual lattice damage resulting from the ion implantation and may increase the strength of the Ni immediately below the precipitates and, thus, extend the optimum strength profile for the implanted layer. As seen in Figure 9, this model reproduces the force and stiffness data well, including the break in the stiffness data at depths beyond 80 nm. The best fit gives a yield strength of 4.15 ± 0.32 GPa, essentially the same as that obtained in our earlier work.[10] Thus, for Ni implanted with both Al and O, annealing at 550 °C does not dramatically reduce the yield strength, in contrast to Ni implanted with O alone. This difference is due to the high thermal stability and resultant absence of ripening of the γ-Al_2O_3 precipitates.

Nanoindentation data for Ni-4 pct Al + O annealed for 2 hours at 550 °C are intermediate between those for Ni-8 pct Al + O and pure Ni. Modeling determined a yield strength of 3.55 ± 0.32 GPa.

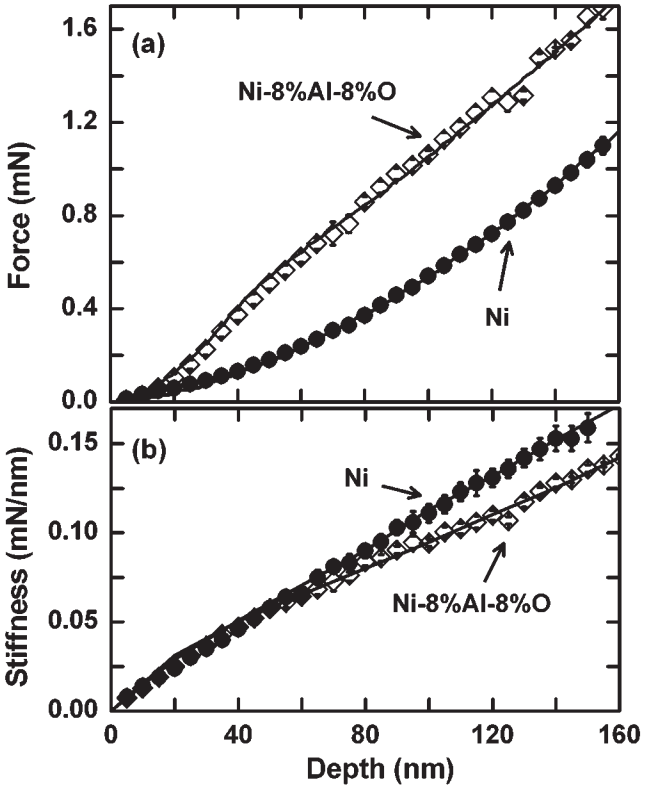

Fig. 9—(*a*) Nanoindentation force and (*b*) stiffness data as a function of depth for Ni-8 pct Al + O, and for pure Ni. Finite-element simulations are shown for both materials.

V. ANALYSIS AND DISCUSSION

The precipitate microstructures and mechanical properties of all of the implanted Ni alloys are summarized in Table III. The two precipitated phases cover a range of volume fractions from 0.053 to 0.30, with sizes from 1.5 nm for as-implanted alloys up to ~20 nm for ripened alloys. Precipitate densities as high as $6 \times 10^{19}/cm^3$ were determined, with edge-to-edge spacings as small as 1.4 nm. The smallest sizes and closest spacings test the applicability of Orowan theory to the nanoscale regime, while inclusion of the ripened alloy tests whether a single mathematical treatment can apply over this broad range of microstructures. These very refined microstructures increased the yield strength to over 5 GPa, or 6.5 pct of the Ni shear modulus.

These broad ranges of microstructure and strength are illustrated in Figure 10. Also included are results obtained with O-implanted Al as obtained by our group earlier,[8,9,42] which are tabulated in Table V. Even smaller precipitates and higher densities were found for the Al alloys. Although our nanoindentation and modeling methods have been refined significantly since the earliest work,[8] the yield strengths did not change significantly when experiments were repeated.[42] Yield strengths with Al are generally less than

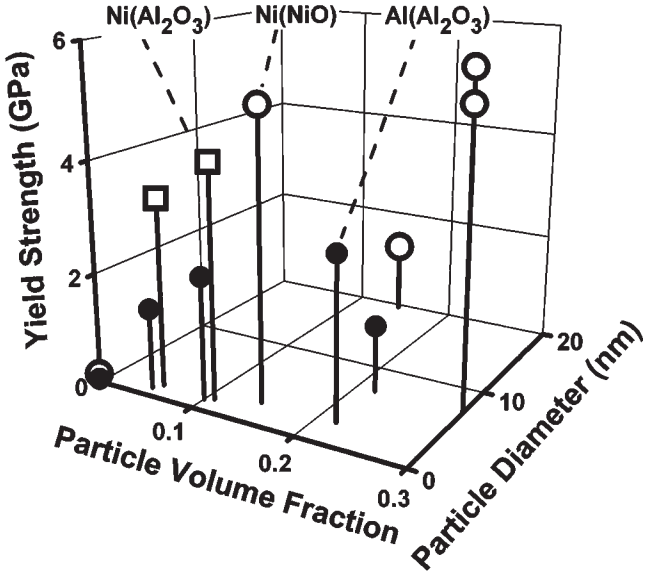

Fig. 10—Three-dimensional plot showing yield strength (vertical height) of ion-implanted alloys as a function of the precipitate volume fraction and diameter (plotted in horizontal plane). Values for Al_2O_3 precipitates in Al matrix are solid symbols; those for Ni are open squares for Al_2O_3 precipitates and open circles for NiO precipitates. Note the broad range of precipitate sizes and volume fractions examined.

Table V. Microstructures and Yield Strengths of O-Implanted Al Alloys*

Specimen Conditions		Precipitate Microstructures					Predicted**
Composition	Anneal	Size (nm)	f	N_v (cm^{-3})	λ (nm)	Yield Strength (GPa)	CRSS (GPa)
Al-20 pct O	none	1.5 to 3.5	0.218	2.7×10^{19}	1.3	2.90 ± 0.40	1.34 ± 0.20
	1/2 h 550 °C	4 to 10	0.218	1.2×10^{18}	3.5	1.20 ± 0.40	0.74
Al-10 pct O	none	0.8 to 1.6	0.100	1.1×10^{20}	1.1	2.20 ± 0.05	0.97
Al-5 pct O	none	0.5 to 1.3	0.048	1.3×10^{20}	1.3	1.45 ± 0.05	0.63 ± 0.05

*Microstructure data and fitted yield strengths compiled from Refs. 8, 9, 12, 30, and 42.
**CRSS values were predicted, as discussed in the text.

those with Ni due to the lower shear modulus of Al. A broad range of sizes and volume fractions also occurs for the γ-Al_2O_3 precipitates in O-implanted Al, with ~1-nm-sized precipitates found at low concentrations and precipitates 7 nm in diameter produced by ripening. Treating the results for the Ni and Al alloys together provides a further test of the theory to scale the results for two metal matrices correctly.

A. *Comparison to Orowan CRSS*

We compare the values for yield strengths determined previously with predicted values based on the precipitate microstructures. For treatment with up-to-date considerations, we follow the theory detailed by Nembach.[6] In it, Orowan's initial result[1] has been mathematically refined in three general areas: (1) interactions between neighboring segments of dislocations bowing around precipitates, (2) random, statistical placement of precipitates in the dislocation path, and (3) inclusion of elastic anisotropy. To treat the statistical nature of precipitate locations, Nembach considers an arbitrarily placed glide plane intersecting an array of spherical precipitates. These intersections are assumed to be circles of radius r_r and to occur on a square lattice with a center-to-center spacing of $L_{\min}$. Incorporating mathematical evaluations of the aforementioned refinements as found in the literature, Nembach obtains (Eq. [6.14b] in Reference 6), for the CRSS to propagate a dislocation,

$$\tau = Y \frac{2K_{Eg}\,(\ln(2D/R_i))}{(L_{\min} - 2r_r)} \left\{ \frac{(\ln(2D/R_i))^{1/2}}{(\ln((L_{\min} - 2r_r)/R_i))^{1/2}} \right\} \quad [7]$$

The prefactor Y (equal to 0.9) allows for randomness of particle arrangement in the glide plane. The term K_{Eg} is the "dislocation-energy parameter" (defined in Eq. [6.2]) that must be evaluated as a geometric mean of the value for edge and screw dislocations. Using Nembach's Eqs. [6.2] and [6.4], we obtain

$$K_{Eg} = \frac{G}{4\pi(1 - \nu)^{1/2}} \quad [8]$$

In Eq. [7], R_i is the dislocation cutoff radius[43] which is equated to the Burgers vector **b**, ν is the Poisson's ratio, and D is defined by

$$1/D = 1/L_p + 1/d_p \quad [9]$$

where $L_p = L_{\min} - 2r_r$ is the edge-to-edge spacing between circular particle intersections of diameter $d_p = 2r_r$ with the glide plane.

Equation [7] is similar to earlier evaluations,[3] but with additional statistical and geometrical corrections. Using D in place of d in the first logarithmic factor extends the interaction between the two dislocation segments passing around a precipitate to include interactions with such segments at neighboring particles. The final factor in braces in Eq. [7] is a geometric factor that results when the interacting dislocation segments on either side of the precipitate are not parallel, and this factor is equal to ~0.9.[6] We have evaluated Eqs. [7] and [9] for a delta-function size distribution with all precipitates having the same diameter, d, as detailed in Chapter 3 of Reference 6. This is the least-complicated distribution and appears reasonable for all our alloys except annealed Ni-8 pct O, for which ripening occurred and produced a range of sizes. We then obtain for the CRSS after algebraic rearrangement:

$$\tau = (0.9)\,\frac{G\mathbf{b}}{2\pi(1 - \nu)^{1/2}}\,\frac{1}{L_p}\,\frac{(\ln(2/b(1/L_p + 4/\pi d)))^{3/2}}{(\ln(L_p/\mathbf{b}))^{3/2}} \quad [10]$$

where L_p in the delta-function approximation is

$$L_p = d((\pi/6f)^{1/2} - \pi/4) \quad [11]$$

The proportionality to $G\mathbf{b}/(1 - \nu)^{1/2}$ is the same as in earlier formulations.[3] The proportionality to $1/L_p$ is similar to the $1/\lambda$ dependence in Eq. [1], but L_p is the edge-to-edge spacing evaluated for precipitates intersecting the randomly placed glide plane; note that the expression for L_p in Eq. [11] differs from our evaluation of λ in Eq. [4].

We evaluated the CRSS for the implanted alloys of Ni and Al using the precipitate parameters in Tables III and V. For Ni, we used $\mathbf{b} = 0.249$ nm and the Reuss-averaged values $G = 77.8$ GPa and $\nu = 0.312$; for Al, the corresponding values are $\mathbf{b} = 0.286$ nm, $G = 26.3$ GPa, and $\nu = 0.347$.[43] The values predicted by Eq. [10] are given in the right-hand columns of Tables III and V. In Figure 11, we have plotted the experimental yield strength for each alloy against the corresponding predicted CRSS value. Error limits are indicated for selected data points; the horizontal error is a range of predicted CRSS values obtained using the observed range of precipitate sizes and possible errors in concentration, *e.g.*, 17.0 ± 1.5 at. pct O for the Ni-16 pct O alloy. A straight line with a slope of 2 accounts well for the data; only one point, that for Ni-8 pct Al + O, lies off the line by more than one error range. A 25 pct change of this slope in either direction would produce a line outside the error ranges of most of the data.

A linear relation between yield strength and calculated CRSS is expected if this evaluation of the Orowan mecha-

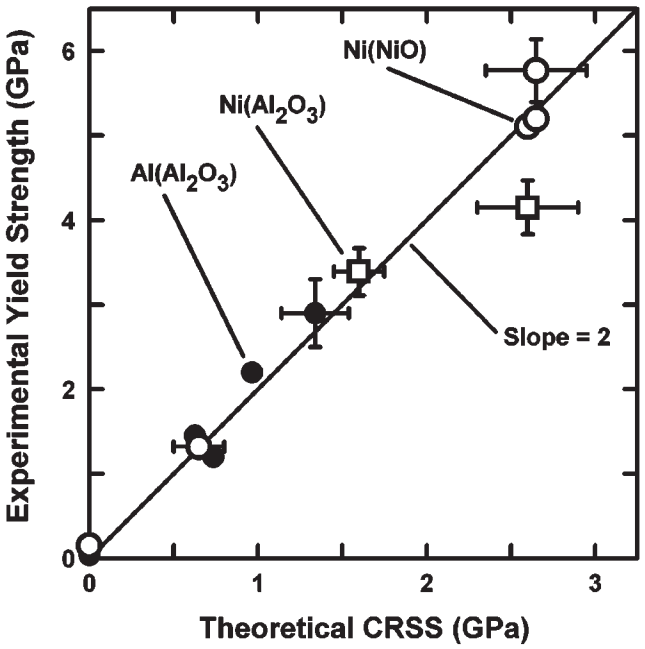

Fig. 11—Plot demonstrating that the experimental yield strength values scale linearly with the CRSS values predicted theoretically with the Orowan mechanism for both Al and Ni implanted alloys. Plotted are values for Al with Al_2O_3 precipitates (filled circles), Ni with Al_2O_3 precipitates (open squares), and Ni with NiO precipitates (open circles). The straight line with slope 2 is seen to relate the two quantities well.

nism applies in our microstructural regime. Our evaluated yield strengths thus indicate that the Orowan formalism can correctly predict how strength varies with changes in microstructure for precipitate sizes and separations approaching ~1 nm. Moreover, the same relation accounts for the results with ripened precipitates and correctly scales results between Ni and Al. In addition, the results for Ni indicate that ~1-nm-diameter precipitates of γ-Al_2O_3 and ~2-nm-diameter precipitates of NiO are effective in blocking dislocation propagation for resolved shear stresses in the material up to 2.65 GPa.

The slope of the line relating yield strength to CRSS in polycrystalline metals is the Taylor factor.[11] By considering the projection of the tensile axis onto available slip systems and averaging over grain orientations, a value of about 3.06 is obtained for uniaxial tensile testing in fcc metals. Our lower value is not unexpected when other experimental results are considered. The tensile tests using copper single crystals with BeO precipitates[4] and with SiO_2 precipitates[5] offer the opportunity to check the theory with known slip orientations. When these experimental results are compared with the aforementioned theoretical evaluation, the observed values are lower by a factor of $\approx$0.6.[6] Such a reduction accounts well for our measured values and the slope we observe: $(3.06) \times (0.6) = 1.8 \approx 2$. In addition, the nature of our indentation testing is sufficiently different from uniaxial tensile testing that agreement with theory may not be exact. The deformations made by indentation are compressive and produce multiple components of stress in the implanted layer and substrate. Our analysis assumes that the von Mises yield criterion[44] correctly considers these components and relates them to the equivalent tensile yield stress. The function used to evaluate the von Mises criterion is empirically chosen and not theoretically derived, but is generally supported by observation. Given these experimental and theoretical considerations, the data for our implanted alloys appear quite consistent with the predictions of Orowan theory.

B. *Comparison to Ideal Shear Strength*

Our observed yield strengths and their agreement with the predictions of Orowan theory imply that the implanted alloys support resolved shear stresses equal to the theoretical CRSS values: up to 2.65 GPa for Ni and 1.35 GPa for Al. These values are 3.4 and 5.1 pct of the corresponding shear moduli, respectively. Such high fractions approach the ideal shear strengths expected for metals. First-order considerations indicate that the theoretical maximum shear strength of crystals is a fraction of the shear modulus:[44] $\tau_{max} = G/2\pi \approx 0.16G$. Recently, density functional theory has been used to calculate the ideal shear strength of fcc Al and Cu at zero temperature with a model that includes atomic relaxation.[45] Values that are 8 to 9 pct of the shear moduli were determined. The authors suggest[45] that scaling to room temperature might reduce the calculated values by a factor of $\approx$2.5,[46] which would give values that are 3 to 4 pct of G. Experiments that used dislocation-free [111] Fe, [111] Cu, and [100] Ag single-crystal whiskers[47] are often considered a good measure of the ideal strength of metals and gave values for τ/G as high as 6.0, 2.2, and 3.1 pct, respectively. The strengths we observe are, thus, approaching limits expected for the maximum shear stresses sustainable by the metal matrices and may provide new insights into these limits. However, for these two-phase alloys, it is not the elemental metal lattice that is required to be stable, but rather the composite material with high densities of coherent or semicoherent precipitates in the metal matrix.

C. *Determination and Comparison of Hardness*

Hardness is commonly used to compare mechanical properties at surfaces, since it can often be obtained by indentation. However, hardness is measured in a condition of large-strain plastic deformation, where the load per contact area increases to an asymptotic value with increasing depth. For indentation partway through implanted layers, where we are most sensitive to their properties, the layer may not be sufficiently plastically deformed, while for greater depths, the measured response of the material is strongly influenced by the softer substrate. To assess implanted layers properly, we need their "intrinsic" hardness, that which would be obtained if a macroscopic piece of the material were indented deeply. One might hope to obtain this by $H \approx 3Y$, but this relation only holds for ductile materials under conditions of fully plastic indentation.[44]

To determine the intrinsic hardness, we use an additional finite-element simulation of indentation into a hypothetical uniform material having the properties of the implanted layer.[12] For instance, for Ni-16 pct O, the layer is assigned a Young's modulus of 263 GPa and a yield strength of 5.77 GPa, as obtained from fitting the indentation data. Simulating indentation of this material to a depth sufficient to allow the force per contact area to reach its assymptotic value gives the intrinsic hardness, 14.5 GPa.

The hardnesses so deduced for implanted Ni alloys are given in Table III. The highest values are 13 to 14 GPa and are somewhat less than 3 times the yield strengths. These values exceed that of hardened 440C bearing steel ($\sim$8 GPa[48]), but not those of hard coatings like TiN or Al_2O_3 (both $\approx$21 GPa[49]). Note that a "rule-of-mixtures" approach does not account for this hardness: the value for annealed Ni-8 pct Al + O is 11.3 GPa, while weighting the hardnesses of implanted Ni and alumina by the appropriate volume fractions gives only

$$(0.89)(2.7) + (0.11)(21.0) = 4.7 \text{ GPa}$$

The intrinsic hardness is, instead, understood to result from blocking dislocation motion with individual precipitates, just as for yield strengths.

D. *Interpreting Young's Modulus*

The fractional increases in the Young's modulus of the implanted alloys are much smaller than those of yield strength. The largest value in Table III is 265 GPa, vs 204 GPa for pure Ni, a 30 pct increase, whereas the yield strength increases by as much as 30 times. In addition, the error limits on the fitted modulus values are sizeable when compared to the increase above pure Ni. These features limit our ability to quantify and understand changes in the modulus. Caution is indicated for as-implanted alloys by the modulus obtained for the Ni-implanted specimen; the central value increases above that of pure annealed Ni, although the error limits include it. Since no new phase is formed with this implantation, no increase in the modulus is expected; the possible increase observed may be the result of lattice damage from the implantation. To reduce possible effects due to implantation damage, we limit our considerations to annealed alloys.

The effective Young's modulus of two-phase composite materials has been derived by Christenson.[50] In the limit of low volume fractions (f) of spherical precipitates with a shear modulus of G_p in a matrix with a shear modulus of G_m and Poisson's ratio of ν_m, he obtains, for the effective modulus of the composite material (Eq. [2.23] of Reference 50):

$$\frac{G}{G_m} = 1 - \frac{15(1 - \nu_m)(1 - (G_p/G_m))\, f}{7 - 5\,\nu_m + 2(4 - 5\nu_m)\,(G_p/G_m)} \qquad [12]$$

Values for the Ni matrix have been provided, while we estimate values for the γ-Al_2O_3 precipitates using those of α-Al_2O_3: $G \approx 160$ GPa and $\nu_p = 0.22$. For Ni-8 pct Al + O, we obtain $G/G_m = 1.076$, which predicts a value for the implanted layer of $E = 220$ GPa, an increase of about one-third that of the fitted value of 255 ± 27 GPa. From this limited assessment, the modulus increases found for implanted alloys appear to be of the correct order, but may be higher than those predicted by elasticity theory. It is possible that approximations made in modeling (such as the von Mises yield criterion, which treats the material as isotropic) and the axisymmetric approximation of the tip shape may limit our ability to evaluate the Young's modulus accurately for thin implanted layers.

VI. CONCLUSIONS AND IMPLICATIONS

We have investigated the strengthening of metal matrices by high volume fractions (up to 0.30) of very small precipitates (down to $\sim$1 nm) and found that recent evaluations of the Orowan mechanism account for the observed yield strengths. In this regime, the Orowan formulation accounts for variations in strength due to changes in precipitate size, density, volume fraction, and metal matrix; it also predicts absolute values for yield strengths within a factor of $\sim$1.5 of our values, similar to agreement in earlier studies.[4,5,6] Agreement was found for both NiO and γ-Al_2O_3 precipitates in Ni and between Al and Ni matrices whose shear moduli differ by 3 times.

While we have shown that our results are consistent with predictions of the Orowan formalism for our microstructures, the question remains whether the exact mechanism of dislocation bowing, looping, and bypassing operates at precipitate sizes and separations as small as $\sim$1 nm. For our high precipitate densities, the precipitate images and the strain fields of dislocations would overlap in projected images obtained by TEM for specimens of reasonable thicknesses, making the identification of loops around precipitates for direct verification of the mechanism very unlikely. It may be possible to detect the mechanism directly for lower densities or larger, ripened precipitates. Dislocation pinning has been detected in Al with much lower densities of large 5 to 20 nm oxide particles that were produced by ion implanting 3 at. pct O and then subjecting the material to a high-temperature laser treatment.[51]

Ion implantation was the key to producing the refined microstructures. However, the thin implanted layers required us to develop special techniques to evaluate their mechanical properties, namely, performing nanoindentation and evaluating the combined response of the layer and substrate with finite-element modeling. This method succeeded in quantifying the yield strength with an overall accuracy of $\sim$10 pct, allowing us to compare results with the Orowan strength mechanism.

Our work clearly demonstrates that implanted Ni layers can be much stronger and harder than other Ni alloys, like the superalloy NIMONIC PE16, with $Y < 1$ GPa.[14] The hardening by oxide precipitates is comparable to that of amorphization of Ni by implanting Ti and C[13] and exceeds that of solution hardening by implanting A1[10] and of radiation damage (refer to the Ni-implanted Ni in Table III). It is notable that Al_2O_3 precipitates in Ni are quite thermally stable, allowing alloys of Ni implanted with Al + O to retain their strength after exposure to temperatures at least as high as 550 °C.

The strongest alloys investigated here have very high yield strengths: $Y \approx 5$ GPa for Ni and $Y \approx 3$ GPa for Al. These strengths result from high values of resolved shear stresses (2.65 and 1.65 GPa) that are 3.4 and 5.1 pct of the shear moduli, respectively. These percentages are in the range of theoretical values for the ideal shear strength of metal lattices.[45] However, in this case, the lattices are two-phase alloys with coherent or semicoherent precipitates, not elemental metals. It appears notable that a 1-nm-diameter γ-Al_2O_3 precipitate contains only 34 O atoms and 23 Al atoms, but, nonetheless, blocks dislocation glide.

These results are potentially important for a new class of devices termed micro-electromechanical systems (MEMS). In one type of MEMS, Ni is being electroformed into high-precision molds to produce miniature components with dimensions ranging from micrometers to millimeters.[52,53]

Methods are being developed to incorporate 25-nm-diameter Al_2O_3 particles into the electroplated Ni to increase its strength.[54] The favorable results we have obtained for Ni with Al_2O_3 precipitates support such efforts, and the thermal stability of our much smaller Al_2O_3 precipitates indicates that the high strength of the electroformed material may be retained after exposure to elevated temperatures. The MEMS components have much higher surface-to-volume ratios than found in conventional-sized devices, and their surface mechanical properties are important because high contact stresses can occur during operation. Implantation treatments like those studied here may, therefore, be useful for hardening the surfaces of Ni components in MEMS.

ACKNOWLEDGMENTS

The authors thank G.A. Petersen for performing the TRIM calculations and ion implantations, as well as measuring composition profiles with ion-beam analysis, and M.P. Moran for preparing the TEM specimens used here. This work at Sandia National Laboratories, a multiprogram laboratory operated by Sandia Corporation, a Lockheed Martin Company, was supported by the Division of Materials Sciences, Office of Basic Energy Sciences, United States Department of Energy, under Contract No. DE-AC04-94AL85000.

REFERENCES

1. E. Orowan: *Symp. on Internal Stresses in Metals and Alloys*, Institute of Metals, London, 1948, p. 451.
2. P.B. Hirsch and F.J. Humphreys: *Proc. R. Soc. London A*, 1970, vol. A318, pp. 45-72.
3. J.D. Embury: *Metall. Trans. A*, 1985, vol. A16, pp. 2191-200.
4. R.L. Jones: *Acta Metall.*, 1969, vol. 17, pp. 229-35.
5. R. Ebeling and M.F. Ashby: *Phil. Mag.*, 1966, vol. 13, pp. 805-34.
6. E. Nembach: *Particle Strengthening of Metals and Alloys*, John Wiley & Sons, New York, NY, 1997.
7. D.M. Follstaedt: in *Materials Science and Technology*, R.W. Cahn, P. Haasen, and E.J. Kramer, eds., VCH Publishers, New York, NY, 1991, vol. 15, pp. 247-87.
8. R.J. Bourcier, S.M. Myers, and D.H. Polonis: *Nucl. Inst. Meth. B*, 1990, vol. B44, pp. 278-88.
9. D.M. Follstaedt, S.M. Myers, R.J. Bourcier, and M.T. Dugger: *Proc. Int. Conf. on Beam Processing of Advanced Materials (1992)*, J. Singh and S.M. Copley, eds., TMS, Warrendale, PA, 1993, pp. 507-17.
10. J.A. Knapp, S.M. Myers, D.M. Follstaedt, and G.A. Petersen: *J. Appl. Phys.*, 1999, vol. 86, pp. 6547-56.
11. G.I. Taylor: *J. Inst. Met.*, 1938, vol. 62, pp. 307-24.
12. J.A. Knapp, D.M. Follstaedt, S.M. Myers, J.C. Barbour, and T.A. Friedmann: *J. Appl. Phys.*, 1999, vol. 85, pp. 1460-74.
13. S.M. Myers, J.A. Knapp, D.M. Follstaedt, and M.T. Dugger: *J. Appl. Phys.*, 1998, vol. 83, pp. 1256-64.
14. E. Nembach and G. Neite: *Progr. Mater. Sci.*, 1985, vol. 29, pp. 177-319.
15. J.F. Ziegler, J.P. Biersack, and U. Littmark: *The Stopping and Range of Ions in Solids*, Pergamon, New York, NY, 1985. The implanted ion distributions in Ni were calculated using the Monte Carlo TRIM-90, provided by J.F. Ziegler, IBM Corporation, Yorktown Heights, NY, private communication, 1990.
16. W.-K. Chu, J.W. Mayer, and M.-A. Nicolet: *Backscattering Spectrometry*, Academic Press, New York, NY, 1978.
17. *SIMNRA Users Guide*, Technical Report No. IPP 0/113, Max-Planck-Institut für Plasmaphysik, Garching, Germany, 1997.
18. M.H. Loretto and R.E. Smallman: *Defect Analysis in Electron Microscopy*, Chapman and Hall, London, 1975, pp. 57-59.
19. *Powder Diffraction File*, International Center for Diffraction Data, Newton Square, PA. fcc Ni: card 04-0850; NiO: card 04-0835; $NiAl_2O_4$: card 10-0339; and γ-Al_2O_3: card 10-0425.
20. J.B. Pethica, R. Hutchings, and W.C. Oliver: *Phil. Mag. A*, 1983, vol. A48, pp. 593-606.
21. M.F. Doerner and W.D. Nix: *J. Mater. Res.*, 1986, vol. 1, pp. 601-09.
22. W.C. Oliver and G.M. Pharr: *J. Mater. Res.*, 1992, vol. 7, p. 1564.
23. G.M. Pharr and W.C. Oliver: *Mater. Res. Soc. Bull.*, 1992, vol. 17 (7), pp. 28-33.
24. All our indentation tests were performed at the Nano Instruments Innovation Center of MTS Systems Corp., Knoxville, TN.
25. ABAQUS version 5.7, Hibbitt, Karlsson & Sorensen, Inc., Pawtucket, RI.
26. *Metals Handbook*, ASM, Metals Park, OH, 1990, vol. 2, pp. 437 and 1143.
27. J. Lubliner: *Plasticity Theory*, Macmillan, New York, NY, 1976.
28. *Atlas of Stress-Strain Curves*, H.E. Boyer, ed., ASM, Metals Park, OH, 1987, p. 551.
29. J.-W. Park and C.J. Altstetter: *Metall. Trans. A*, 1987, vol. A18, pp. 43-50.
30. D.M. Follstaedt, S.M. Myers, and R.J. Bourcier: *Nucl. Instrum. Meth. B*, 1991, vols. B59-B60, pp. 909-13.
31. D.A. Porter and K.E. Easterling: *Phase Transformations in Metals and Alloys*, Van Nostrand Reinhold, Wokingham, England, 1981. This text discusses the thermodynamics and structural considerations of precipitation; chapter 3 on interfacial energies and chapter 5 on nucleation.
32. *Handbook of Chemistry and Physics*, R.C. Weast and M.J. Astle, eds., CRC Press, West Palm Beach, FL, 1978, p. D-67. The heat of formation of γ-Al_2O_3 is -385 kcal/mole.
33. W. Gust, M.B. Hintz, A. Lodding, H. Odelius, and B. Prendel: *Phys. Status Solidi A*, 1981, vol. A64, pp. 187-94.
34. R.A. Swalin and A. Martin: *Trans. AIME*, 1956, vol. 206, pp. 567-72.
35. W.H. Gitzen: *Alumina as a Ceramic Material*, American Ceramic Society, Columbus, OH, 1970, pp. 3 and 29. Note that the γ-Al_2O_3 phase is referred to as η in this reference.
36. M. Nastasi, J.-P. Hirvonen, T.T. Jervis, G.M. Pharr, and W.C. Oliver: *J. Mater. Res.*, 1988, vol. 3, pp. 226-32.
37. N.A. Fleck, G.M. Muller, M.F. Ashby, and J.W. Hutchinson: *Acta Metall. Mater.*, 1994, vol. 42, pp. 475-87.
38. N.A. Stelmashenko, M.G. Walls, L.M. Brown, and Y.V. Milman: *Acta Metall. Mater.*, 1993, vol. 41, pp. 2855-65.
39. M.S. De Guzman, G. Neubauer, P. Flinn, and W.D. Nix: *Mater. Res. Soc. Symp. Proc.*, 1993, vol. 308, pp. 613-19.
40. Q. Ma and D.R. Clarke: *J. Mater. Res.*, 1995, vol. 10, pp. 853-63.
41. W.D. Nix and H. Gao: *J. Mech. Phys. Solids*, 1998, vol. 46, pp. 411-25.
42. J.A. Knapp, D.M. Follstaedt, J.C. Barbour, and S.M. Myers: *Nucl. Instrum. Meth. B*, 1997, vols. B127-B128, pp. 935-39.
43. J.P. Hirth and J. Lothe: *Theory of Dislocations*, 2nd ed., Krieger, Malabar, FL, 1992, pp. 63-64 and 836-37.
44. F.A. McClintock and A.S. Aragon: *Mechanical Behavior of Materials*, TechBooks, Fairfax, VA, 1966, pp. 118, 276-79, and 453-58.
45. D. Roundy, C.R. Krenn, M.L. Cohen, and J.W. Morris: *Phys. Rev. Lett.*, 1999, vol. 82, pp. 2713-16.
46. A. Kelly and N.H. Macmillian: *Strong Solids*, 3rd ed., Clarendon Press, Oxford, UK, 1986.
47. S.S. Brenner: *J. Appl. Phys.*, 1956, vol. 27, pp. 1484-91.
48. L.E. Pope, F.G. Yost, D.M. Follstaedt, J.A. Knapp, and S.T. Picraux: in *Wear of Materials 1983*, K.C. Ludema, ed., ASME, New York, NY, 1983, pp. 280-87.
49. H. Holleck: *J. Vac. Sci. Technol. A*, 1986, vol. A4, pp. 2661-69.
50. R.M. Christensen: *Mechanics of Composite Materials*, John Wiley & Sons, New York, NY, 1979, pp. 31-52.
51. S. Bader, P.A. Flinn, E. Arzt, and W.D. Nix: *J. Mater. Res.*, 1994, vol. 9, pp. 318-27.
52. E.W. Becker, W. Ehrfeld, P. Hagmann, A. Maner, and D. Münchmeyer: *Microelectron. Eng.*, 1986, vol. 4, pp. 35-56.
53. H. Guckel, K.J. Skrobis, J. Klein, and T.R. Christenson: *J. Vac. Sci. Technol. A*, 1994, vol. A12, pp. 2559-64.
54. T.E. Buchheit, J.R. Michael, S.H. Goods, R.P. Janek, and P.T. Kotula: Sandia National Laboratories, Albuquerque, private communication, 2002.